Sensitivity analysis in core diagnostics

(article starts on next page)

Sensitivity analysis in core diagnostics

J. Herb [a], Y. Périn [a], S. Yum [b], A. Mylonakis [c], C. Demazière [c,*], P. Vinai [c], M. Yu [d], J. Wingate [d], M. Hursin [e]

[a] Gesellschaft für Anlagen- und Reaktorsicherheit (GRS) gGmbH, Boltzmannstr. 14, 85748 Garching bei München, Germany
[b] Technische Universität München (TUM), 85748 Garching bei München, Germany
[c] Department of Physics, Chalmers University of Technology, SE-412 96 Gothenburg, Sweden
[d] University of Lincoln, Brayford Pool, LN6 7TS Lincoln, UK
[e] Laboratory of Reactor Physics and Systems Behaviour, École Polytechnique Fédérale de Lausanne (EPFL), 1015 Lausanne, Switzerland

ARTICLE INFO

ABSTRACT

In the CORTEX project, methods to simulate neutron flux oscillations were enhanced and machine-learning based tools to determine the causes of measured neutron flux oscillations were developed, using the results of simulations as training and validation data. For a selected combination of those methods and tools, several sensitivity analyses were performed to assess their robustness and trustworthiness. The neutron flux oscillations were simulated using the tool CORE SIM+. It calculates the three-dimensional field of the neutron flux oscillations, which can be used to determine the response of neutron detectors at given locations. For the sensitivity analysis, the neutron flux oscillations were assumed to be caused by the vibration of one fuel element. It was investigated how selected input parameters like the core loading pattern, the burn up of the fuel elements, the neutronic core data, the geometry details of the vibrating fuel element, the chosen detectors, and other noise source parameters like the amplitude of the fuel element vibrations, affect the simulated neutron flux oscillations. A three dimensional fully convolutional neural network had been developed and trained during the CORTEX project to determine the cause and location of perturbations causing given measurements of in-core detectors in pressurized water reactors. The robustness of this network was tested by applying it to the simulated detector readings created during the sensitivity analysis.

1. Introduction

In the CORTEX project, different machine learning techniques have been developed to identify the causes of neutron flux noise in research and power reactors. These methods are based on their training with simulated noise data for the corresponding reactors for a defined set of possible causes. The inputs for the methods are measurements of the thermal neutron noise at given detector locations.

For a power reactor, it is not possible to create a complete training/validation set of all possible causes of the noise (including variations of the exact definition of the source, the characteristics of the detectors, the operational conditions, and other factors) by only relying on measured plant data. The reason lies with the impossibility of controlling the perturbations and, if they exist, the absence of their knowledge and characteristic features. The training and validation of machine learning-based techniques thus need to be based on simulation data for postulated anomalies. To assess the quality and robustness of the machine learning tools, it is therefore of interest to determine their sensitivity to different factors like the exact definition of the neutron noise source, the characteristics of the detector and changes in the simulation setup used for training/validation.

Among the machine learning methods developed in CORTEX are deep neural networks which identify the cause of neutron flux oscillations and their location inside the reactor based on the thermal neutron flux measured by in-core detectors of a pressurized water reactor (PWR). One example of such a deep neural network is the three dimensional fully convolutional neural network (3D-FCNN) to which the sensitivity analyses is applied in this paper. It was trained for a special PWR with 36 in-core neutron flux detectors. To train this 3D-FCNN, neutron flux noise simulations for different operational states and different neutron noise

causes had been performed. Then the neutron flux at the detector locations was extracted to be used for the training.

To assess the sensitivity of the trained neural network, it was first investigated how sensitive the used simulation tool itself reacts to changes in different simulation parameters. These parameters are related to nuclear data, the source of the neutron noise and the detectors to measure the noise. The influence of these factors on the noise was quantified and the factors were ranked. In a second step, it was investigated how robust the 3D-FCNN can identify the noise source if simulation results based on these varied inputs were fed as input.

The paper is organized in the following way. Section 2 introduces the simulation method for the neutron flux, the methodology of the sensitivity analysis, the assumption to create the inputs of the sensitivity analysis, and the setup of neural-network-based machine learning method. In Section 3 the results of the sensitivity analysis applied first to the simulation tool of the neutron flux and then on the neural network are determined and discussed. The paper ends with some conclusions and outlook.

2. Methodology and preparation of analysis

2.1. Modelling of reactor neutron noise

The target reactor considered hereafter is the Gösgen Nuclear Power Plant, also referred to as 'Kernkraftwerk Gösgen (KKG)'. The plant is located in the Däniken municipality in Switzerland. It is operated by the Kernkraftwerk Gösgen-Däniken AG since the start of its operation in 1979 (Kernkraftwerk Gösgen-Däniken AG (KKG), 2016). The reactor is licensed to operate at a nominal thermal power of 3002 megawatts. The reactor is a pressurized water reactor delivered by German Kraftwerk Union AG. It contains 177 fuel assemblies (with control rods that can be inserted in 48 of those assemblies). Each fuel assembly contains 205 fuel rods, which consist of enriched UO2 fuel with fissile uranium-235 or MOX fuel with a proportion of fissile plutonium. However, MOX fuel has not been used since 2012.

In the context of the CORTEX project, the Paul Scherrer Institute (PSI) provided the necessary core data, which include three-dimensional distribution of the nodal macroscopic cross-sections in two-energy groups and the kinetic parameters. Different core conditions and cycles were considered: cycle 39 (Middle Of Cycle – MOC and End Of Cycle – EOC) and cycle 40 (Beginning Of Cycle – BOC, MOC and EOC). The analyses reported hereafter are based on these core conditions and cycles.

As mentioned earlier, the detection of anomalies in power reactors can be most efficiently carried out by first building a database of spatial neutron noise responses for various postulated anomalies, and then building a machine learning architecture aimed at identifying, from the plant measurements, the spatial neutron noise pattern resembling a postulated anomaly. For creating the necessary database, simulations are used, as annotated plant data, i.e., plant measurements for which the anomaly is known, do not exist or are not available.

The modelling of neutron noise can be performed in various ways, depending on the level of refinement in the representation of the spatial, angular, and energy variables associated to the neutron flux. Moreover, the simulations can be performed either in the time-domain or in the frequency-domain, using either deterministic or probabilistic (i.e., Monte Carlo) methods, using linear theory or not.

Nevertheless, as the number of simulations required to build the database is extremely large, fast running algorithms are required. In the present work, the CORE SIM+ code is thus used for the generation of the database. It is a frequency-domain code relying on the two-group diffusion equation in linear theory (Mylonakis, et al., 2021). Regarding the spatial discretization, finite differences are used. Although the core is typically represented by a set of large homogeneous regions, of typical characteristic length in the range of 10 cm, the use of finite differences requires a mesh size of 1–2 cm for guaranteeing the accuracy of the solution. Moreover, and as will be illustrated hereafter, noise sources are defined on very small subdomains. CORE SIM+ makes thus use of dedicated numerical techniques that allow to refine the mesh in some selected parts of the system. We refer to (Mylonakis, et al., 2021) for further details on CORE SIM+.

In the present analysis, the following types of noise sources were considered and modelled in CORE SIM+:

· Generic "absorber of variable strength", where a spatial Dirac-like perturbation is assumed. All possible locations of the perturbation were considered for frequencies ranging from 0.1 to 25 Hz.
· Axially travelling perturbations at the velocity of the coolant flow, where a perturbation is created at some spatial location in the core and travels upwards with the flow through the core. All possible locations of the perturbation were considered for frequencies ranging from 0.1 to 25 Hz.
· Fuel assembly vibrations, for which the lateral movement of fuel assemblies was modelled according to the following modes of vibrations: the cantilevered beam mode (for frequencies ranging from 0.6 to 1.2 Hz), the simply supported on both sides mode (with its two first harmonics – frequencies ranging from 0.8 to 4.0 Hz for the first mode and frequencies ranging from 5.0 to 10.0 Hz for the second mode), and the combined simply supported and cantilevered beam mode (with its two first harmonics – frequencies ranging from 0.8 to 4.0 Hz for the first mode and frequencies ranging from 5.0 to 10.0 Hz for the second mode) (see Fig. 1). All possible locations of the vibrating fuel assembly were modelled.
· Control rod vibrations, where a partially inserted control rod is assumed to laterally vibrate in the core. All possible locations of the vibrating control rod were considered for frequencies ranging from 0.1 to 20.0 Hz.
· Core barrel vibrations, where the core barrel was assumed to vibrate in the beam or pendular mode for frequencies ranging from 7 to 13 Hz.

The generation of the spatial noise responses as described above are detailed in (Mylonakis, et al., 2021).

For the considered reactor, the creation of the database was carried out at four core conditions: Mid of Cycle 39 (MOC39), End Of Cycle 39 (EOC39), Beginning Of Cycle 40 (BOC40) and End Of Cycle 40 (EOC40).

In the following of this paper, one out of the considered scenarios described above is also given special attention, as the parameters used for defining the noise source were perturbed, with the objective to perform a sensitivity analysis on those. Moreover, the impact of such perturbations onto the results of the machine learning unfolding will be assessed in the remaining of this paper. The scenario singled out corresponds to fuel assembly vibrations. Only one vibrating fuel assembly and one oscillation mode were considered: the cantilevered beam mode at a frequency of 1 Hz. The axial shape of the displacement for that kind of oscillation is given as defined in (Demazière & Dokhane, 2019):
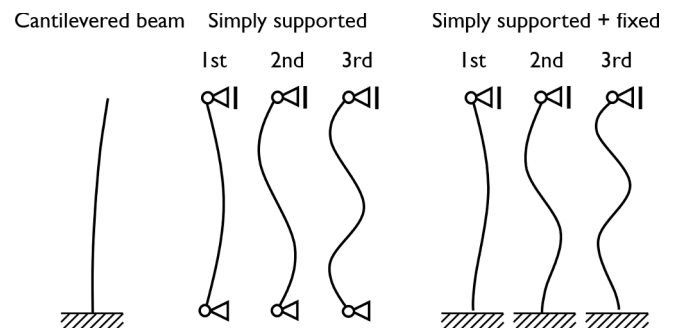

Fig. 1. Idealized fuel assembly oscillation modes (Bläsius et al., 2022).

$$\{\cos(\kappa_1 z) - \cosh(\kappa_1 z) - \gamma_1 [\sin(\kappa_1 z) - \sinh(\kappa_1 z)]\}$$

with $\kappa_1 = \dfrac{1.8751}{H}$ and $\gamma_1 = \dfrac{\cos(\kappa_1 H) + \cosh(\kappa_1 H)}{\sin(\kappa_1 H) + \sinh(\kappa_1 H)}$ (1)

In the equations above, z represents the axial elevation in the core and H is the core height. The axial shape of the displacement is given in Fig. 2, together with the radial location of the moving assembly. The moving assembly is located at equilibrium position 53.9 cm from the center of the core, whereas the vibration is assumed to only occur along the *x*-direction.

In terms of CORE SIM+ nodalization, $76 \times 51 \times 102$ nodes are used to represent the core in the *x*-, *y*- and *z*-directions, respectively. The area around the neutron noise source is modelled with refined mesh cells of size 4.3 mm, whereas the other parts of the core have mesh sizes varying between 3 and 10 cm. Fig. 3 shows the nodalization of the core at the axial mid-point.

2.2. Methodology of sensitivity analysis

Various correlations which measure the influence of a given input parameter to an output variable, and consequently, rank the importance of input parameters, can be applied for sensitivity analyses. Amongst the available options, the Pearson Correlation Coefficient (PCC) is selected for sensitivity measures because of its simplicity. The availability and the compatibility that PCC has in analysing the correlation between the input and output parameters under the neutron noise condition have been confirmed in (Yum, et al., 2022). The PCC is a measure of linear correlation between two sets of data and its value is estimated as the covariance of the two sets, divided by the product of their standard deviations (Conover, 1980) (Anon., n.d.). The PCC (commonly represented by the Greek letter ρ) between two random variables (X, Y) can be defined as follows:

$$\rho_{X,Y} = \frac{cov(X, Y)}{\sigma_X \sigma_Y}$$ (2)

where cov is the covariance and σ_X and σ_Y are the standard deviations of X and Y, respectively.

Additionally, a Z test is carried out to determine whether the obtained correlation coefficients are statistically significant. The test requires the setting of a significance level, i.e., a threshold of probability that is used to decide whether the null hypothesis (the coefficients are significant) is accepted or rejected. Following a general guideline, the significance level is taken as 5 % and, given an estimation of PCC based
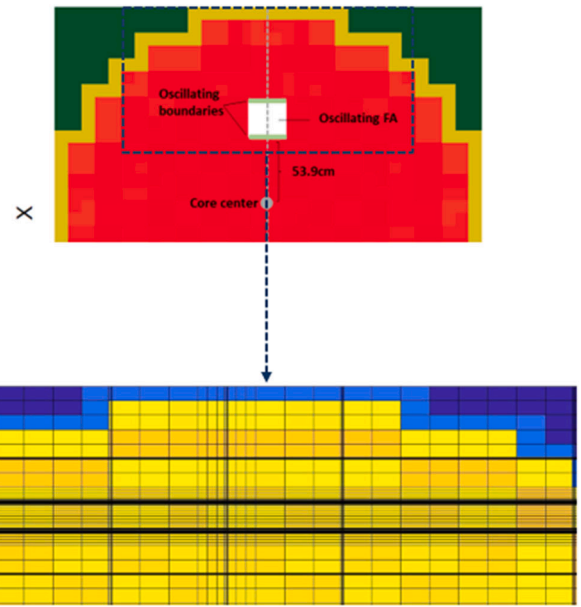

Fig. 3. Description of the radial nodalization around the noise sources at mid-core elevation.

on samples of 300 values, this leads to a critical value equal to 0.11 (Ramsey, 1989) (Kajuri, 2018). This means that, if the absolute value of the PCC calculated with samples of 300 values is larger than 0.11, the input and output variables can be regarded as "correlated" with a 5 % probability that the result is not true (95 % confidence level).

As a last step, the calculated coefficient is squared to represent the "sensitivity index", which expresses what fraction of the variation of the dependent variable is explained by the variation in the independent variable (Bluman, 2009).

2.3. Inputs for sensitivity analyses (nuclear uncertainties, oscillation parameters, reactor/measurement geometry

Fig. 4 shows a schematic flow chart of the developed methodology, including the expected outcomes from each step. The subsections below describe the important points involved in the various steps.

The final output (neutron noise) is a complex quantity, since CORE SIM+ performs the calculation in the frequency domain. Therefore, the complex values are converted into amplitude and phase of neutron noise
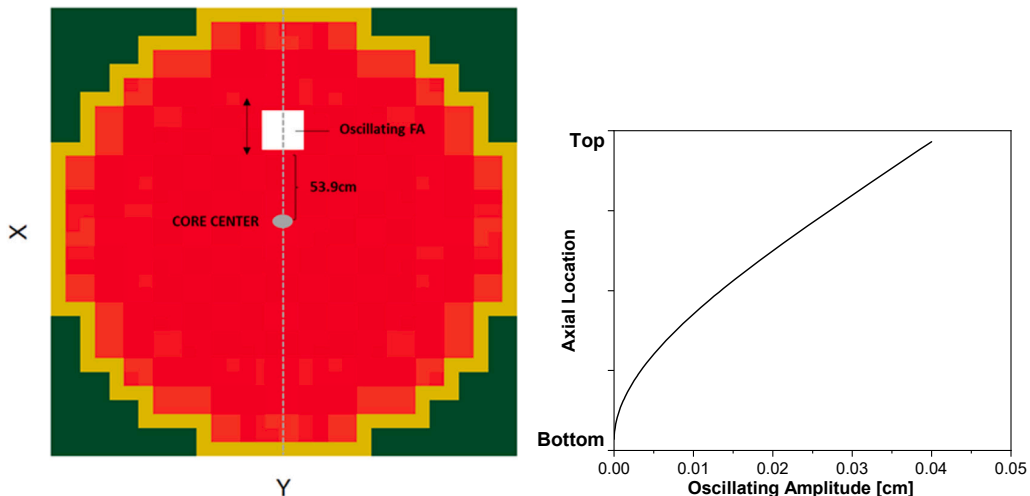

Fig. 2. Radial location of the considered vibrating assembly (left) and axial shape of the maximum lateral displacement of this assembly.
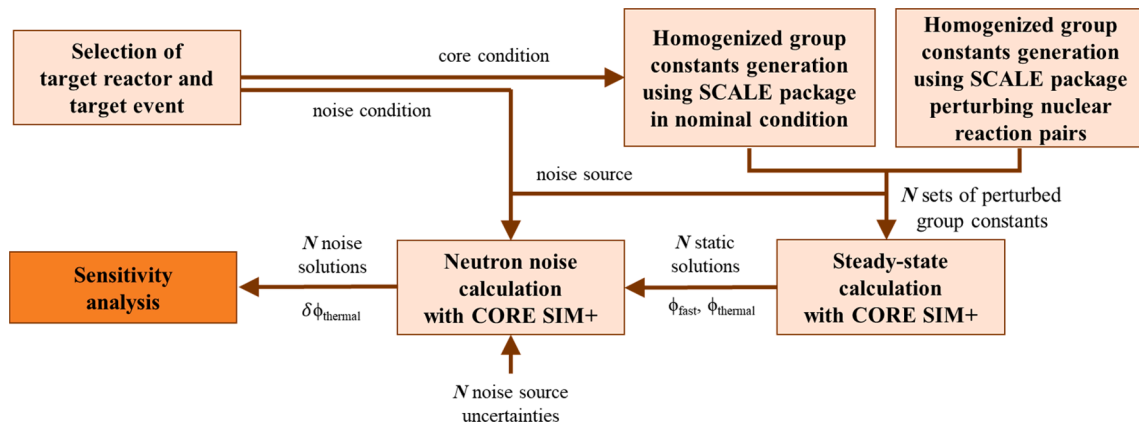
Fig. 4. Flow chart for the sensitivity analysis.

via post-processing. The focus of the current study is limited to the thermal neutron noise since the detectors in the reactor are essentially sensitive to thermal neutrons.

2.3.1. Uncertain parameters

The input parameters for the target reactor and transient are investigated according to expert judgement as summarized in Table 1. The distribution information of each input parameter was defined in some earlier work (Yum, et al., 2022). The oscillating amplitude and frequency are thus perturbed with a standard deviation of 5 % around their nominal values, while the specific location (noise source and detectors) is perturbed with an uncertainty of 1 mesh around its ideal location. The scope of the present work is a sensitivity analysis to identify the most important input parameters. An uncertainty analysis to quantitatively assess its results would require a more detailed analysis of the distributions of the input parameters.

The Swiss 3-loop pre-Konvoi reactor KKG has a total of 36 in-core neutron detectors. They are installed in 6 different axial positions and each axial position consists of 6 detectors in different radial positions, see Fig. 5 (Gösgen, 2018). In the simulations, the 36 detecting locations are perturbed between -1 mesh and $+1$ mesh from the ideal locations,

Table 1
The distribution information of selected uncertain parameters.

Parameter	Distribution	Unit	Mean	Standard deviation[2] (Lower/ Upper limit[3])
Nuclear data[4]				
Oscillating amplitude	Normal	cm	Inherent oscillating curve in Fig. 2	5 %
Oscillating frequency	Normal	Hz	1	0.05
Location of noise source	Uniform	Mesh	Ideal oscillating boundary	$-1/+15$
Detecting location (x-axis)	Uniform	Mesh	Ideal detecting location	$-1/+1$
Detecting location (y-axis)	Uniform	Mesh	Ideal detecting location	$-1/+1$
Detecting location (z-axis)	Uniform	Mesh	Ideal detecting location	$-1/+1$

[1]This column shows the value of lower and upper limit in case of having uniform distribution.
[2]Nuclear data uncertainties are treated in a distinct manner and the detailed information regarding the uncertainty propagation process is provided in Section 2.3.2.
[3]$-1/+1$ correspond to $-0.43/+0.43$ cm.
[4]The computation time is identical for all core conditions and fuel cycles.

in the $x-$, $y-$ and $z-$ directions.

2.3.2. Generation of random samples

In the Simple Random Sampling (SRS) method, random sets of perturbed input parameters are generated using the distribution information listed in Table 1. The nuclear data uncertainties are treated in a distinct manner, which is described thereafter.

The direct treatment of the nuclear data uncertainty would lead to a very large number of uncertain parameters (e.g., in the covariance data provided by SCALE: 94 nuclides, typically 2–8 reactions per nuclide, 44 energy groups per reaction). CORE SIM+ uses 2-energy group, homogenized macroscopic nuclear parameters, which are: D_{fast}, $D_{thermal}$, $\Sigma_{abs,fast}$, $\Sigma_{abs, thermal}$, $\Sigma_{nufis, fast}$, $\Sigma_{nufis, thermal}$, Σ_{rem}. The uncertainties of the nuclear data are propagated to the macroscopic nuclear parameters needed for CORE SIM+ simulations in order to study their impact.

For this purpose, the SAMPLER module from the SCALE code package is applied. SAMPLER is a stochastic uncertainty quantification tool (Rearden & Jessee, 2016) sections, fission yield, decay data, and any user input parameter of a SCALE component. This study only considers the neutron cross section uncertainty. This is achieved by using the master sample file included in SCALE. This master file contains 1000 samples of perturbation factors for all energy groups and reactions in all materials. These factors have been pre-computed with the Medusa module of the XSUSA program using the 44-group covariance data provided by SCALE using the 44-group covariance data provided by SCALE.

All SCALE models use thermal–hydraulic conditions representative of core-averaged conditions at Hot Full Power, namely a fuel temperature of 900 K and a moderator density of 707 kg/m^3. Since all the fuel assembly types from these two cycles differ only slightly in enrichment, two SCALE fuel assembly models are considered using the minimum and maximum enrichments (4.90 % and 5.06 %) found in cycles 39 and 40. No information is available regarding the burnup distribution for either cycle. Therefore, the effect of burnup on the neutron cross section uncertainty is treated by considering fresh fuel and fuel at 30 MWd/tHM. The test matrix presented in Table 2 gives a representation of which parameter combinations are studied.

In total 300 varied macroscopic cross-sections were generated using SAMPLER for each of the 3 cases presented above. From those 300 samples of macroscopic cross-sections, relative variations from the reference version of the nuclear data libraries are computed and are applied to vary the macroscopic cross sections for CORE SIM +. The standard deviation of ratios between the samples and the reference case is presented in Table 3. The standard deviations remain low (maximum < 0.3 %) for all group constants. The effect of the burnup on the standard deviation is larger than the effect of the enrichment. The resulting sensitivity of the neutron noise phase and amplitude is presented in the following sections.
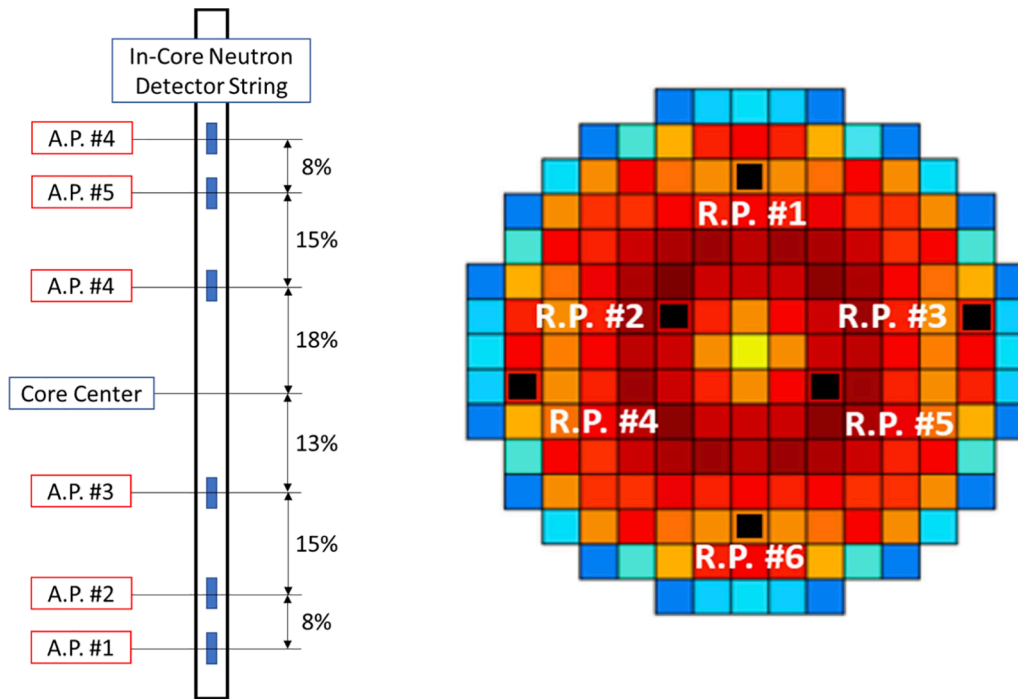
Fig. 5. Locations of in-core detectors in axial and radial direction of the core. On the left: values in percent (%) indicate "% active fuel length"; "A.P." and "R.P." denote "axial position" and "radial position", respectively.

Table 2
Test matrix.

	Fuel burnup	
Enrichment	5.06 % Enrichment @ 0MWd/t Burnup 4.9 % Enrichment @ 0MWd/t Burnup	5.06 % Enrichment @ 30MWd/t Burnup

2.4. Setup of deep neural network and its training

To classify and localize multiple, simultaneously occurring perturbations in the nuclear core, we borrow the idea of semantic segmentation. In our case, each semantic label represents the perturbation scenario, with its location in the volume/voxel (i, j, k) in a nuclear core representing where this perturbation originated. For achieving semantic segmentation (working out which perturbation scenario occurs at which volume/voxel), a 3D Fully Convolutional Neural Network (3D-FCNN) as in (Durrant, et al., 2019), has been developed as shown in Fig. 6. From comprehensive evaluation/comparison studies in (Durrant, et al., 2019), it has been shown that the 3D-FCNN can effectively classify/locate various types of perturbation types effectively.

Compared with other deep learning techniques (Caliva et al., 2018; Demazière et al., 2020), the 3D-FCNN technique (Durrant, et al., 2019) can classify/locate the occurrence of multiple simultaneous perturbations in the core. And as in (Durrant, et al., 2019), the 3D-FCNN achieves a very high accuracy (more than 99 %) for perturbation detection based on 44 ex/in-core sensors.

The network follows a traditional encoder-decoder structure found in semantic segmentation. The encoder extracts and constructs high-dimensional spatial feature representations of the frequency domain input volume, whilst the decoder utilizes these features to construct a prediction mask with the same dimensions as the input, indicating the types of perturbation in different voxels/volumes in the core. Both the encoder and decoder are constructed of 3D CNN layers, which are ideal for learning spatial information to extract representative features.

The model proposed is inspired from (Kaul, et al., 2020) by introducing the spatial pyramid pooling block (four bottom blocks of the network), which learns rich semantic features at various scales, using four CNN layers with differing kernel size, stride, and dilation to capture varying information at different granularities. Additionally, to capture greater spatial information given the limited number of detectors, dilated convolutions (Wang, et al., 2019) are employed to increase the receptive field of the convolution operator whilst maintaining computational efficiency.

The 3D-FCNN is trained to minimize the below focal loss between a voxel-wise prediction and ground truth semantic labels. The stochastic gradient descent (SGD) algorithm is applied for minimizing the loss function.

$$\mathcal{L}_{FL}(y,\widehat{y}) = -\frac{1}{P}\sum_{p=1}^{P}\left[y_p\alpha_p\left(1-\widehat{y}_p\right)^{\gamma}\log\left(\widehat{y}_p\right) + \left(1-y_p\right)\left(1-\alpha_p\right)\widehat{y}_p^{\gamma}\log\left(1-\widehat{y}_p\right)\right]$$

(3)

3. Results of the analysis

To confirm how the core condition affects the sensitivity of input parameters to the neutron noise, three out of five core conditions

Table 3
Propagation of nuclear data uncertainty to nuclear parameters for CORE SIM+ (standard deviation of ratios between 300 samples and nominal case).

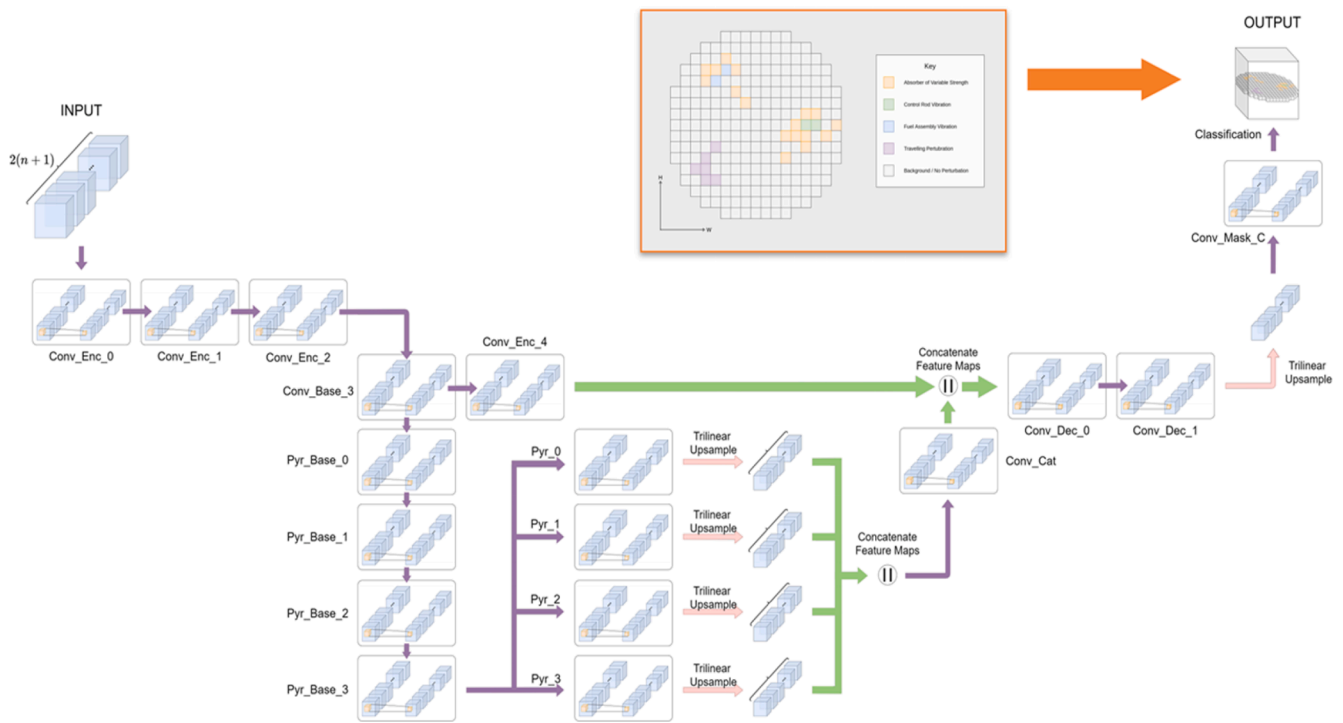|	D_{fast}	$D_{thermal}$	$\Sigma_{abs,\,fast}$	$\Sigma_{abs,\,thermal}$	$\Sigma_{nufis,\,fast}$	$\Sigma_{nufis,\,thermal}$	Σ_{rem}
5.06 %@0MWd/t	4.35E-04	9.22E-04	4.12E-03	7.07E-04	2.63E-03	1.32E-03	1.16E-03
5.06 %@30MWd/t	4.85E-04	8.17E-04	4.10E-03	7.73E-04	2.18E-03	2.11E-03	1.50E-03
4.9 %@0MWd/t	4.37E-04	9.20E-04	4.18E-03	7.02E-04	2.62E-03	1.31E-03	1.16E-03

Fig. 6. The sketch diagram of the 3D-FCNN architecture.

provided (see Section 2.1) are selected from the viewpoint of fuel loading pattern and fuel burn-up: to check the influence of loading pattern, EOC 39 and EOC 40 are selected, while BOC and EOC in cycle 40 are considered to confirm the fuel burnup effect. For the noise simulation with CORE SIM+ at each core condition, the homogenized nuclear data generated at the corresponding condition are used as nominal data.

Meanwhile, in (Yum & Perin, 2021), it is confirmed that neither a core condition considered to generate the nuclear data uncertainties, nor a way to apply the nuclear data uncertainties to fuel rods (an identical uncertainty for all FAs or different uncertainty for each FA) does affect the results in a significant manner. Accordingly, further analyses at BOC and EOC will only consider the nuclear data uncertainties generated at the core conditions of 5.06 %-wt & 0 MWd/t and 5.06 %-wt & 30 MWd/t (introduced in Section 2.3.2), respectively, assuming that all the fuel assemblies have identical nuclear data uncertainties. These combinations are made to perform the analysis at the specific core condition with

the nuclear data uncertainties generated from the burnup condition mostly similar to the given core condition within the available options suggested in Table 2.

3.1. Convergence/sensitivity test

A series of convergence tests are performed by varying the sample size. This test is necessary to find out an optimal sample size which strikes a balance between computational cost and reliability of the calculated sensitivity index. The tests are carried out with different sample sizes between 10 and 500, which are sampled randomly from 500 existing data sets, under the conditions of BOC 40. The sampling of equivalent sample size is repeated for 1000 times using bootstrapping with replacement (Sarrazin, et al., 2016). Afterwards, the 2.5th and 97.5th percentile of the 1000 sensitivity indices are identified to build 95 % confidence interval. Fig. 7 shows the converging trend of two
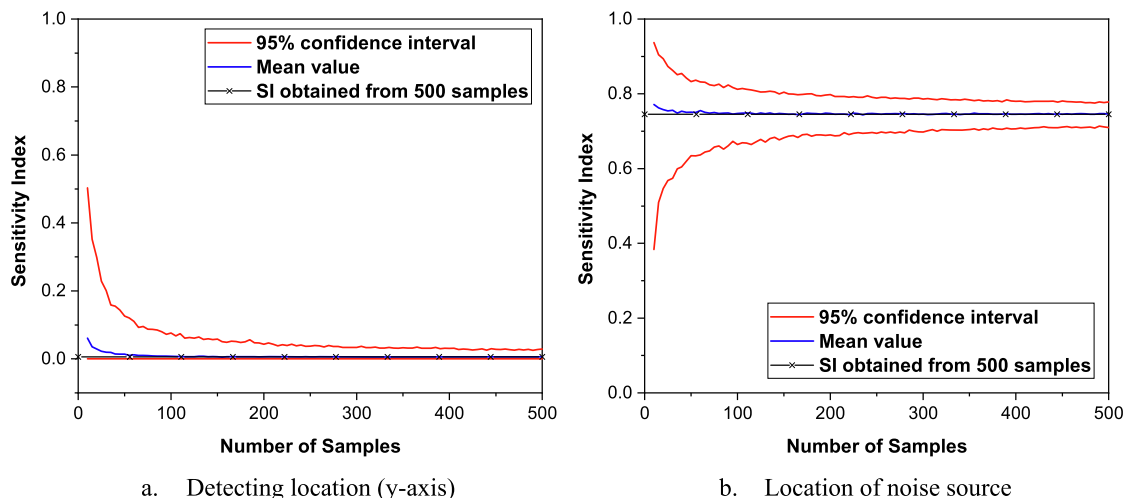

a.   Detecting location (y-axis)

b.   Location of noise source

Fig. 7. Convergence of sensitivity indices with 95% confidence interval ("SI" denotes "sensitivity index").

representative sensitivity indices to the amplitude of the thermal neutron noise: "detecting location (y-axis)" which has relatively small index and "location of noise source" which has relatively large index at the detector location of A.P. #1 and R.P. #2.

The confidence interval decreases as the sample size increases. When the sample size is larger than 300, the difference between the calculated confidence interval (with a sample size larger than 300) and the final estimation with 500 samples becomes smaller than 0.15. Considering the small difference with the final estimation, the further analyses will be carried out using a sample size of 300 whose computation time is equivalent to 2.5 days for both steady-state and noise calculation.[1]

3.2. Results from sensitivity analysis

3.2.1. Analysis at BOC 40

Fig. 8 shows the radial distribution of the thermal neutron noise in the core for the nominal condition without uncertainties.

To get a better understanding on the noise behaviour at the detector locations, correlation matrices for the amplitude and phase of the thermal neutron noise are calculated based on 300 data sets as shown in Fig. 9 (Yum & Perin, 2021). This correlation information helps to infer the noise behaviour at the specific detector location by reading the signals from the correlated detectors. Additionally, it enables to perform the group-wise uncertainty analyses, which simplifies the interpretation process of the calculation results.

In case of the amplitude of thermal neutron noise, the detectors can be radially divided into three groups according to three different correlations: group 1 consists of the signal at the radial position #1, group 2 consists of the signals at the radial positions #2, #5 and #6, group 3 consists of the signals at the radial positions #3 and #4.

Meanwhile, the phase data show simpler correlations than the amplitude data. The data at radial positions #2 to #6 have almost perfect positive linear correlations among each other and have perfect negative linear correlations with the value at radial position #1. The latter is explained by the out-of-phase behaviour existing between the radial position #1 and all other radial positions, as shown in Fig. 8b.

Since correlations exist between the thermal neutron noise at the detector locations, the uncertainties of the noise (distribution range of the neutron noise) are also expected to show correlated responses at the detector locations. That is, when the signals from two detectors are correlated, their uncertainties respond in the same direction, either increase or decrease, as the input parameters are perturbed. As a result, the correlated detector signals are expected to have similar sensitivities to the input parameters, which will be investigated in the following sections.

Simplified approach with grouped parameters

A groupwise sensitivity analysis is conducted to investigate the relative effects of the different groups of parameters. The 13 input parameters listed in Table 1 are grouped into three groups according to the similarities they have in between: (1) group of nuclear data, (2) group of noise source data, (3) group of detecting locations. The group of detector locations includes the perturbation of the location in the x −, y − and z − directions. The group of noise source data includes the oscillating amplitude, the oscillating frequency, and the location of the noise source. The uncertainties of thermal neutron noise obtained for the three different groups are compared in Fig. 10. The neutron noise is calculated with the perturbation of parameters belonging to a given group, while the remaining input parameters are fixed at their nominal values. The neutron noise uncertainties are obtained following 1st order Wilks' formula for two-sided limits, for which the required number of code runs corresponds to 93.

The graph showing the results for the detector locations consists of 6 blocks along the x − axis (Fig. 11), where each block corresponds to each

axial position shown in Fig. 5. Each block contains the values from the 6 radial detectors located in this axial position and the corresponding radial position is represented with ascending order, from position #1 (very left value in the block) to #6 (very right value in the block).

For both the amplitude and phase of the neutron noise, the uncertainties propagated from the group of noise source data show the largest value in all detector locations, while they are followed by the uncertainties from the group of nuclear data. The uncertainties by group of nuclear data become larger at radial position #3 at low axial positions, still, they are not remarkably different from the uncertainties from the group of noise source data. Accordingly, the obtained results can be simply interpreted as the neutron noise being mainly driven by the group of noise source data.

Approach with quantitative measure

Based on the results obtained from the simplified approach, an additional analysis with quantitative measure is carried out. Here, the parameter which contributes to the neutron noise the most within the group of noise source data is quantitatively identified. This can be done by calculating the sensitivity indices for each input parameter. The calculated sensitivity indices between the three noise source parameters and the neutron noise are summarized in Fig. 12 and Fig. 13 with 95 % confidence intervals.

The main findings can be explained in connection with the correlation among the detector locations shown in Fig. 9. For the neutron noise amplitude, the oscillating amplitude dominates in all axial positions at radial position #1, while the location of the noise source is always dominating at radial positions #3 and #4. However, at radial positions #2, #5 and #6, the location of noise source dominates at the lowest position and becomes weaker at higher axial positions. The decreasing effect is caught up by the increased effect of the oscillating amplitude and at higher axial locations, eventually, the oscillating amplitude becomes the main contributor.

The phase data at all detector locations are strongly dependent on the location of noise source, which supports the correlation information shown in Fig. 9.

3.2.2. Analysis at EOC 40

The sensitivity analysis with an identical procedure as the one adopted in Section 3.2.1 is repeated at the core conditions of EOC 40. The different core conditions are reflected in the different values of the two-group nuclear data of the core, resulting in different noise behaviour as shown in Fig. 14. The considered event (one FA oscillation) in this study brings about a larger amplitude of neutron noise at the core condition of EOC 40 than at BOC 40 (see Fig. 8).

Problematic point in analysis

As shown in Fig. 8-b and Fig. 14-b, CORE SIM + predicts an "out-of-phase" behaviour between two core regions because of a vibrating fuel assembly. The boundary of these two regions is determined by the location of the noise source, which is one of the input parameters considered in this study. However, the boundary reacts sensitively to the uncertainty of the noise source location, although this uncertainty corresponds to only ±4.3mm. The modification of the boundary can change the phase region that the detector actually sees, therefore, it can affect the phase signal measured by the core detectors. Fig. 15 shows the variation of the boundary according to the perturbation of the noise source location at the bottom position of the detector installation (Yum & Perin, 2021): radial positions #2, #4 and #5 can belong to two different phase regions depending on the location of noise source.

Consequently, when the location of the noise source is perturbed 300 times within its uncertainty range, the obtained 300 noise solutions at these problematic detectors' locations show a discontinued distribution as shown in Fig. 16. The histogram of amplitude data confirms that if a certain location may belong to two different phase regions depending on the change of the oscillating boundary, the amplitude also encounters a similar issue, which results in a discontinuity of the calculated data.

The discontinuity existing among the calculated output data makes it

---

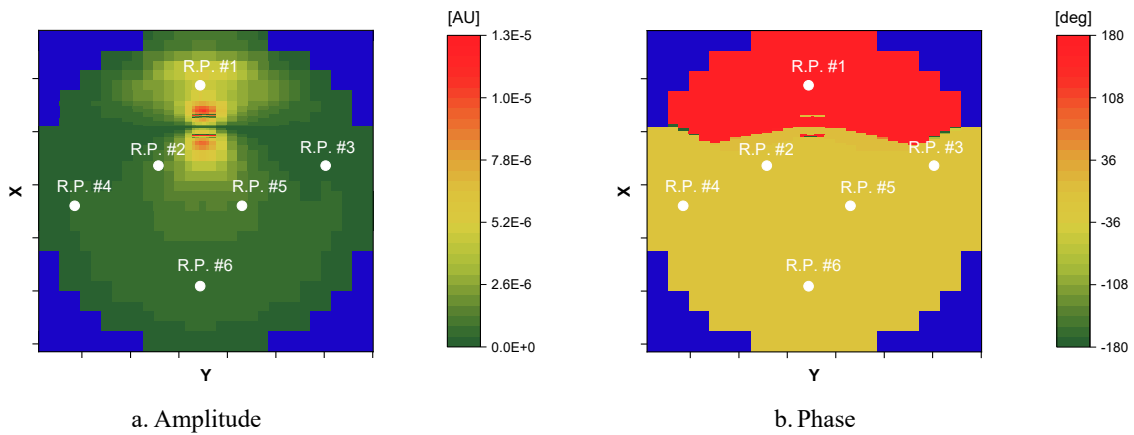[1] The computation time is identical for all core conditions and fuel cycles.

a. Amplitude

b. Phase

Fig. 8. Thermal neutron noise at the axial position #3 at BOC 40.
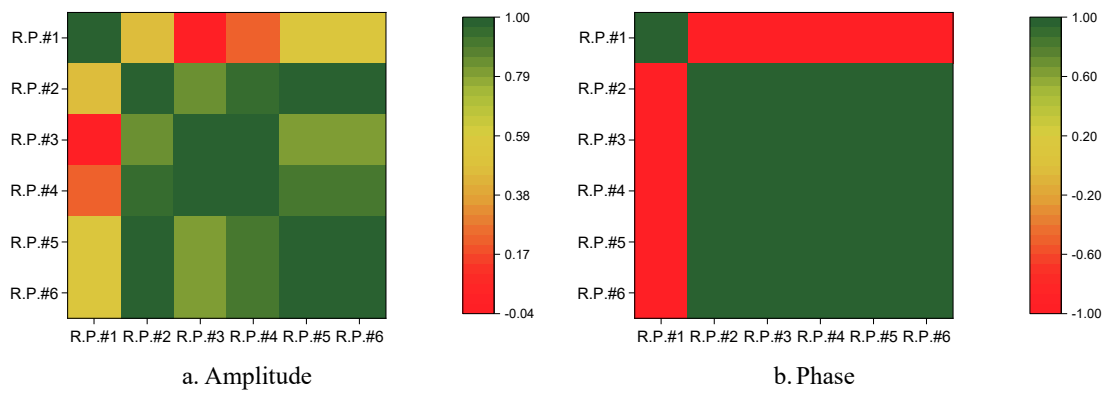

a. Amplitude

b. Phase

Fig. 9. Correlated behaviour between the amplitude and the phase of the thermal neutron noise at the detector locations at axial position #3 (Yum & Perin, 2021).
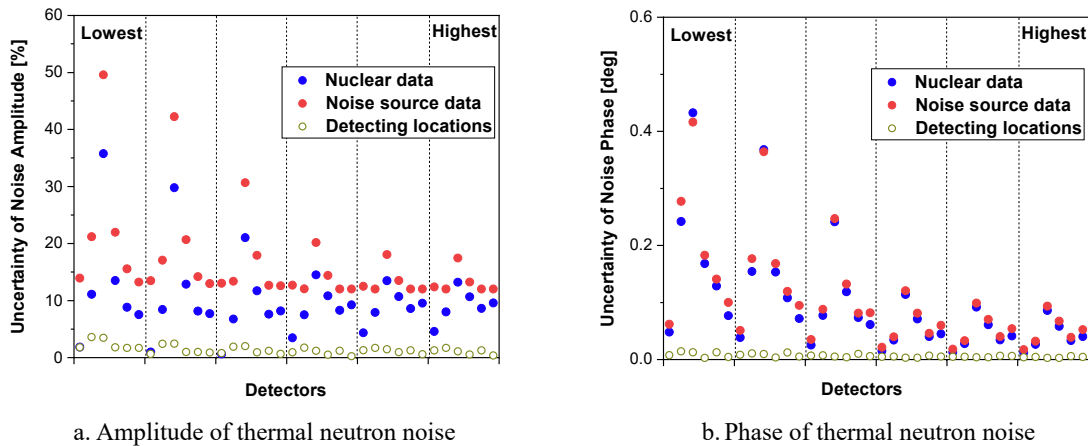

a. Amplitude of thermal neutron noise

b. Phase of thermal neutron noise

Fig. 10. Comparison of neutron noise uncertainties obtained from the different groups of input parameters.

impossible to adopt the regression-based approach for the further sensitivity analysis, since this approach is only valid on the premise that there is a linear relationship between the inputs and the outputs. Accordingly, the following sensitivity analysis is carried out only for the detectors which are not having this property (i.e., radial positions #1, #3 and #6).

Approach with quantitative measure

For the sake of conciseness, only the results of the noise source data are dealt with hereafter and discussed. The sensitivity indices are calculated and compared to those at BOC 40 in Fig. 17 and Fig. 18, in order to understand the findings in connection with an effect of "fuel burnup". The comparison is made only at the radial locations where the relevant sensitivity indices at EOC 40 are available, namely R.P. #1, #3 and #6.

First of all, the noise signals at the detector locations which are excluded here (radial positions #2, #4 and #5) are more sensitive to the location of the noise source than any other input parameters. That is, despite not carrying out further statistical analysis with the data at the radial positions #2, #4, and #5, the main contributing parameter at these locations can be determined as being the location of noise source.
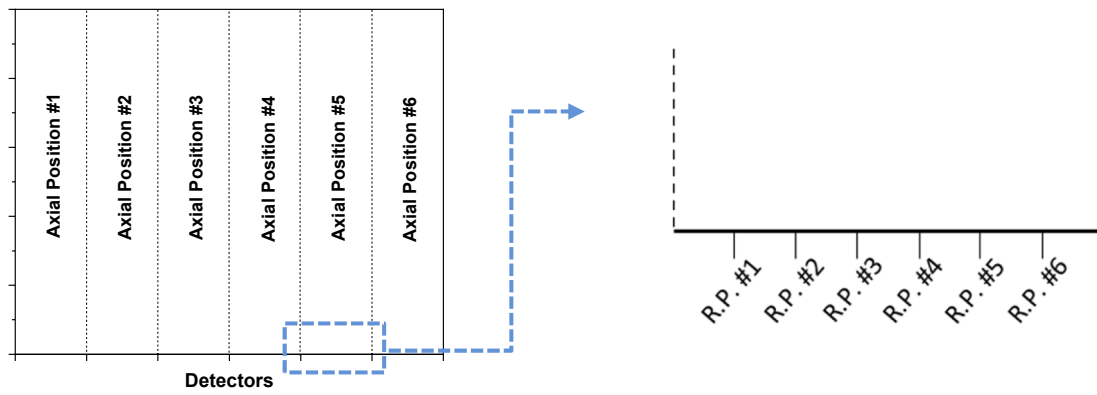
Fig. 11. The composition of the graph with respect to the detector information ("R.P." denotes "Radial position").

a. Oscillating amplitude   b. Oscillating frequency   c. Location of noise source
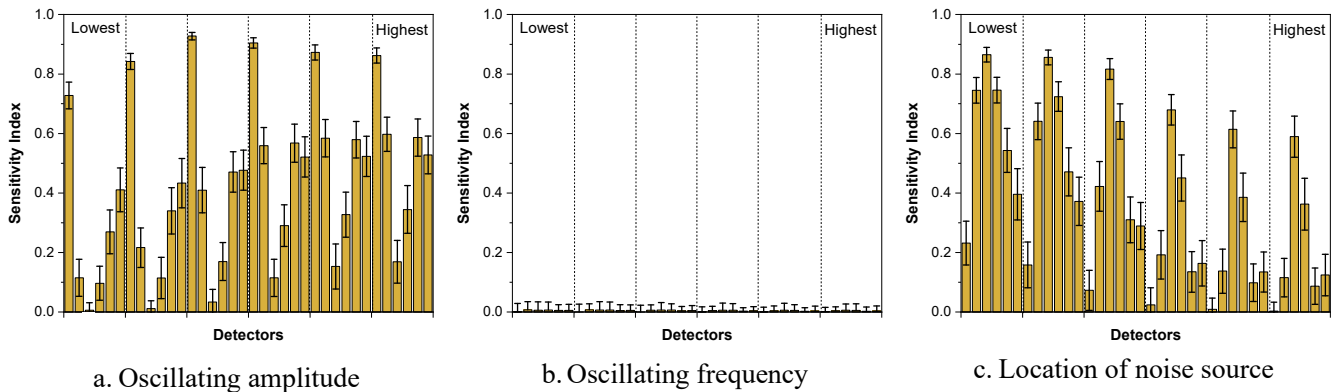
Fig. 12. The sensitivity indices and the 95% confidence intervals between noise source parameters and thermal neutron noise amplitude at different detector locations at BOC 40.
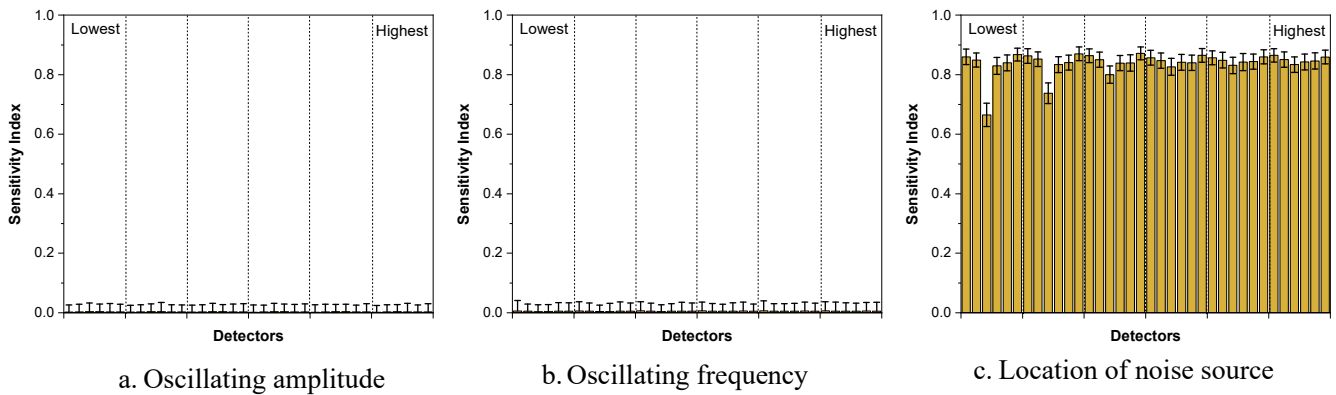

a. Oscillating amplitude   b. Oscillating frequency   c. Location of noise source

Fig. 13. The sensitivity indices and the 95% confidence intervals between noise source parameters and thermal neutron noise phase at different detector locations at BOC 40.

In Fig. 17, the oscillating amplitude becomes less influential at EOC, while the effect from the location of the noise source is increased in most detector locations. Meanwhile, there is no remarkable change in the phase (Fig. 18), and the location of the noise source still maintains its dominant effect. A possible reason why the influence from the location of the noise source at EOC has been increased will be discussed in Section 3.3.

3.2.3. Analysis at EOC 39
Fig. 19 shows the distribution of the thermal neutron noise in the radial core direction under unperturbed conditions.
Problematic point in analysis

The same issue as reported at EOC 40 is found at EOC 39 with a different pattern as shown in Fig. 20. The problematic point is found at the radial position #1 between the mid-height and the top of the core (Yum & Perin, 2021). Therefore, the following sensitivity analysis is carried out for all detectors except for those at radial position #1.
Approach with quantitative measure
To study the effect of fuel loading pattern, the sensitivity indices obtained for the case of EOC 39 are compared with those for EOC 40. Only the radial locations with relevant sensitivity indices are taken, i.e., RP #3 and #6. The results at each axial point are shown in Fig. 21 and Fig. 22.
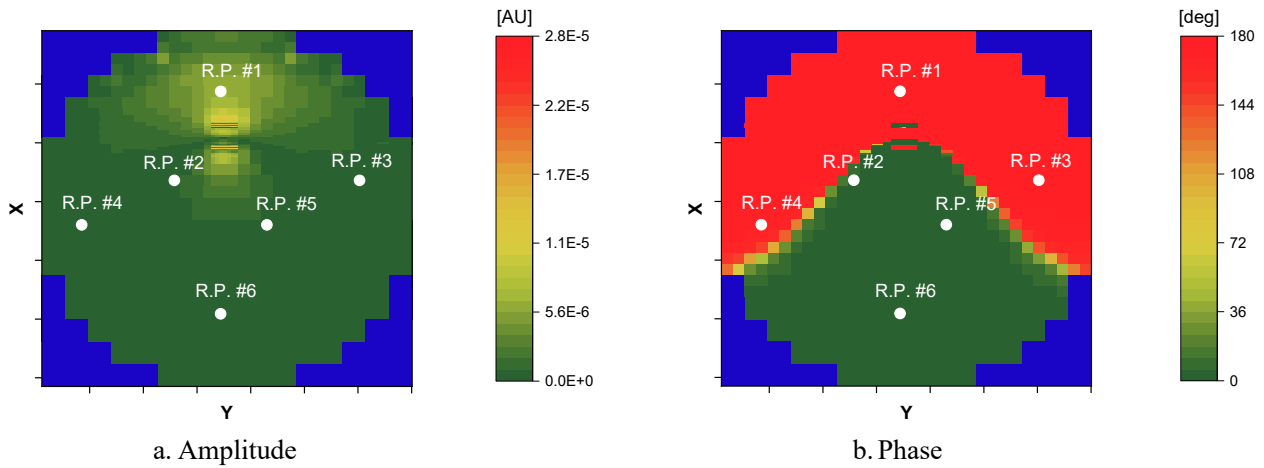Contrary to the results between different fuel burnup conditions (see

a. Amplitude

b. Phase

Fig. 14. Thermal neutron noise at the axial position #3 at EOC 40.

a. 1 mesh toward core periphery

b. Ideal position
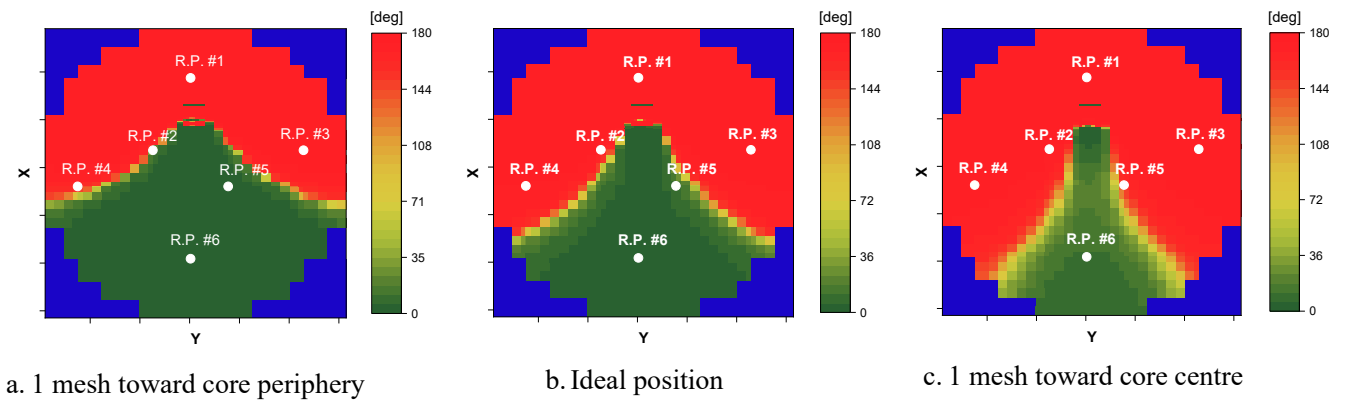
c. 1 mesh toward core centre

Fig. 15. The phase of thermal neutron noise depending on the location of noise source at EOC 40 (at the bottom position of the detector installation).
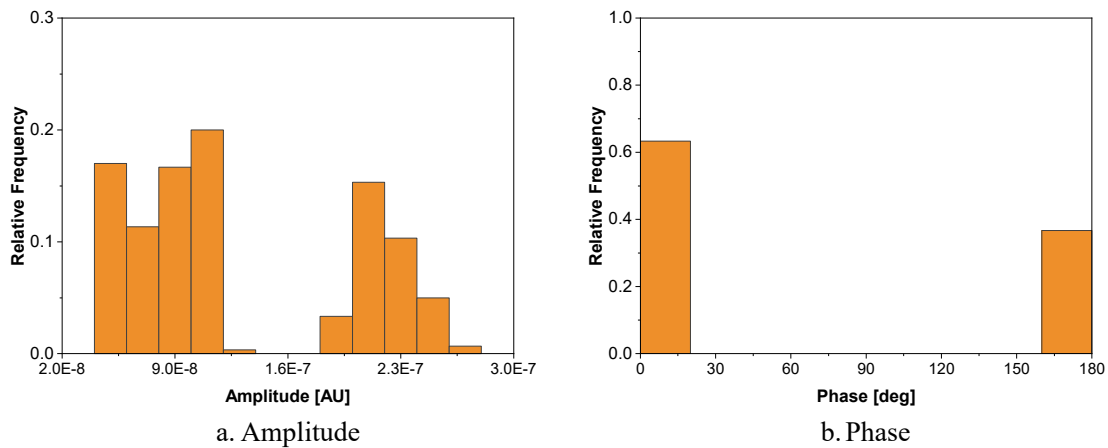

a. Amplitude

b. Phase

Fig. 16. Histogram of 300 thermal neutron noise at the location of detector 4 (at the mid-height position of the detector installation) (Yum & Perin, 2021).

Fig. 17), only monotonous changes are found in Fig. 21. The oscillating amplitude at EOC 39 affects the amplitude of the noise in a significant manner, nonetheless, the location of noise source maintains its dominant effect at both core conditions. In the case of the phase (see Fig. 22), the oscillating frequency shows a visible influence at EOC 39, which decreases as the detecting position gets higher axially. However, the phase of neutron noise is mainly driven by the location of noise source at both EOC 39 and EOC 40. The following section discusses why the location of noise source remains as a main contributor to the neutron

noise at EOC.

3.3. Comparison between different cycles and reasons for differences

A reason why the location of noise source at EOC has an increased influence on the neutron noise compared to BOC can be investigated in relation to the spatial distribution of the static flux. Both the static fast and the static thermal neutron fluxes affect the neutron noise in combination with the noise source. Depending on the position of the noise
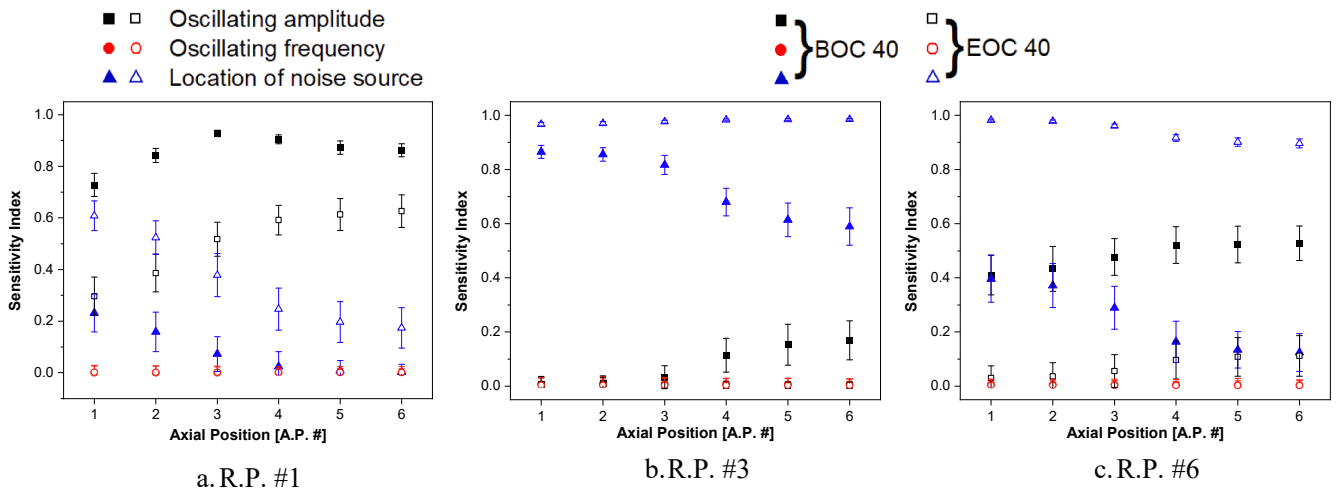
Fig. 17. Comparison of sensitivity indices and the 95% confidence intervals at different radial and axial locations between BOC 40 and EOC 40 (amplitude).
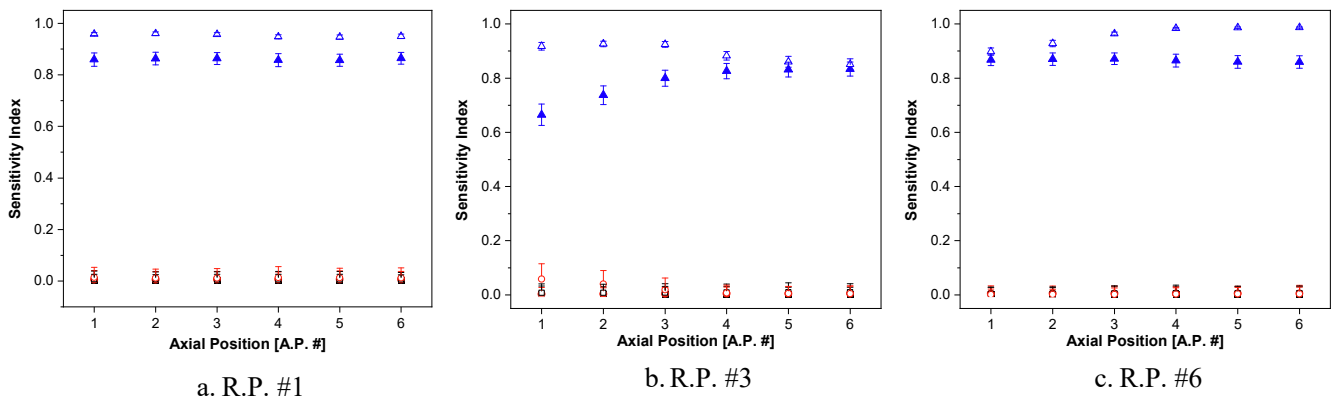

Fig. 18. Comparison of sensitivity indices and the 95% confidence intervals at different radial and axial locations between BOC 40 and EOC 40 (phase).
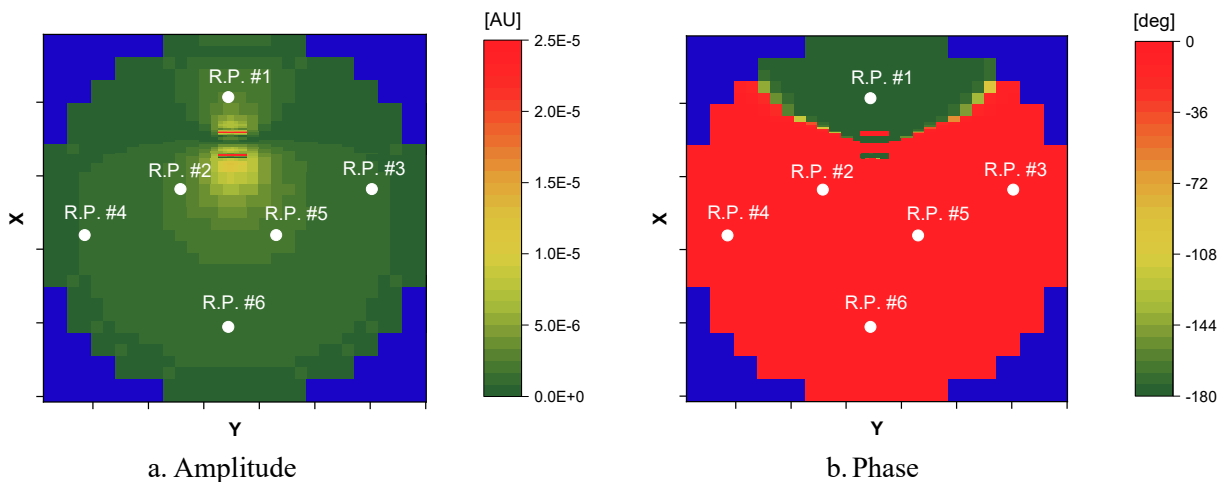

Fig. 19. Thermal neutron noise behaviour at the axial position #3 at EOC 39.

source, the static flux can provide a different weight because of its spatial distribution. Accordingly, the gradient of the static flux is investigated within the uncertainty range of "location of noise source" in order to compare the "weighting factors" between two different core conditions: BOC and EOC. Fig. 23-a shows the perturbation of the oscillating boundary in two-dimensional meshes. "0 mesh" indicates the

ideal location of the oscillating boundary without uncertainty perturbation, while "-1 mesh" and "+1 mesh" denote the relocation of the oscillating boundary by −1 (to the core periphery) mesh and +1 (to the core centre) mesh, respectively. The ratios of static flux gradients between the adjacent two meshes (between −1 mesh and 0 mesh, and between 0 mesh and +1 mesh) are compared in Fig. 23-b (BOC 40 and
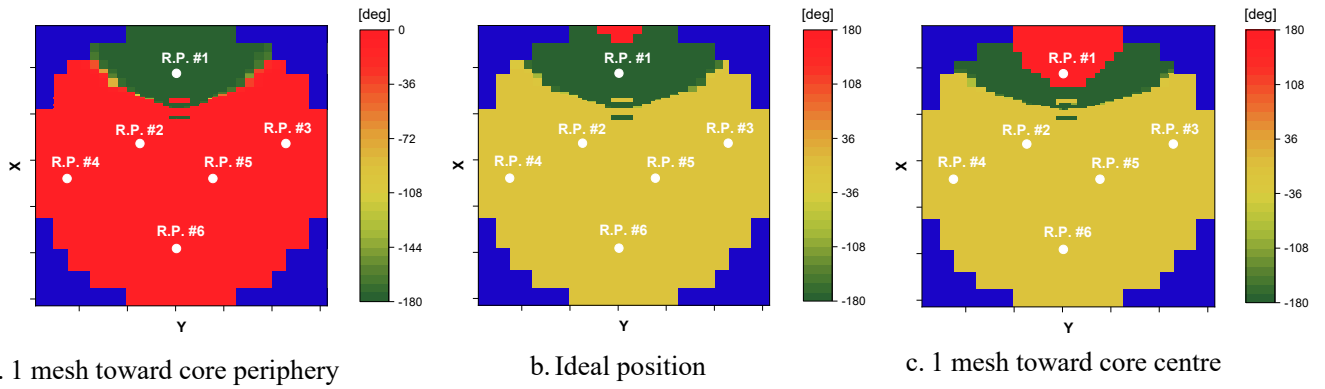
a. 1 mesh toward core periphery   b. Ideal position   c. 1 mesh toward core centre

Fig. 20. The phase of thermal neutron noise depending on the location of the noise source at EOC 39 (at the mid-height position of the detector installation).
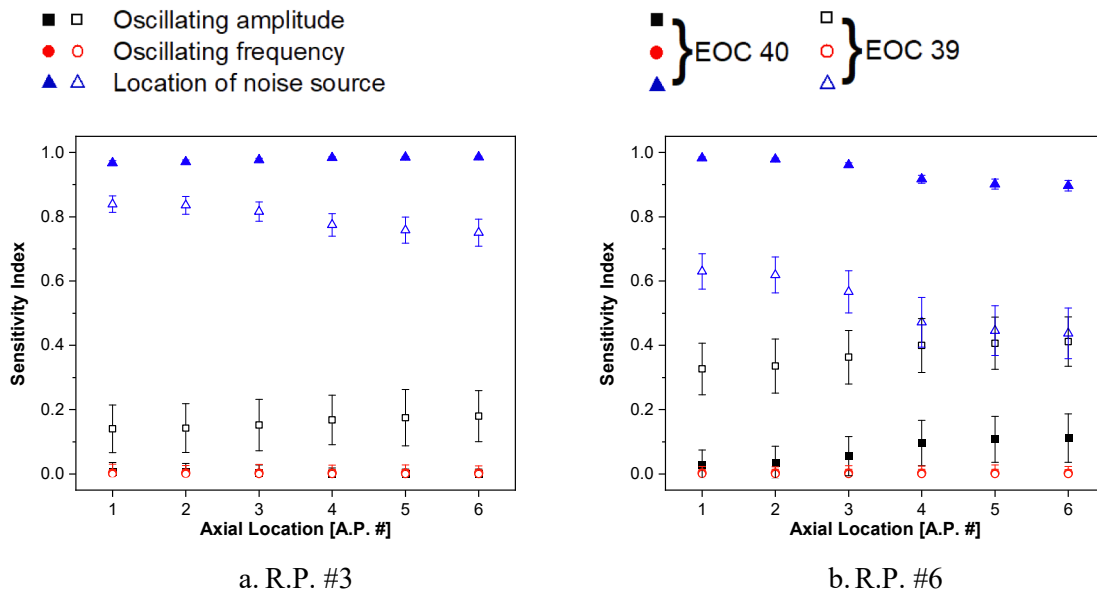

a. R.P. #3   b. R.P. #6

Fig. 21. Comparison of sensitivity indices and the 95% confidence intervals at different radial and axial locations between EOC 39 and EOC 40 (amplitude).

a. R.P. #3   b. R.P. #6
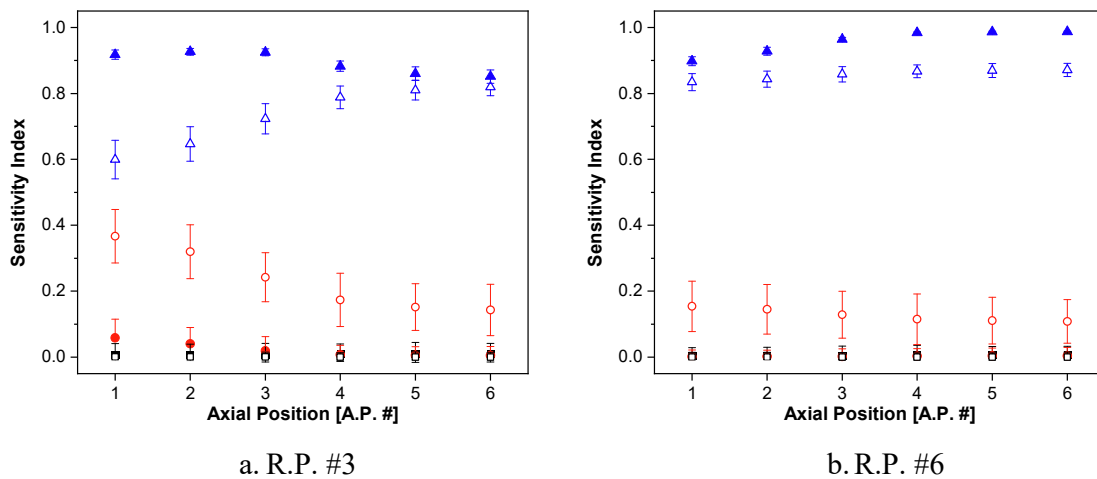
Fig. 22. Comparison of sensitivity indices and the 95% confidence intervals at different radial and axial locations between EOC 39 and EOC 40 (phase).

EOC 40) and Fig. 23-c (BOC 40 and EOC 39).

A value larger than 1.0 signifies that the static flux gradient at EOC (cycle 40 and 39 in Fig. 23-b and -c, respectively) is larger than that at BOC. In most axial locations, both fast and thermal static fluxes at EOC have steeper gradients around the oscillating boundaries than at BOC 40. Consequently, the noise source at the oscillating boundaries at EOC

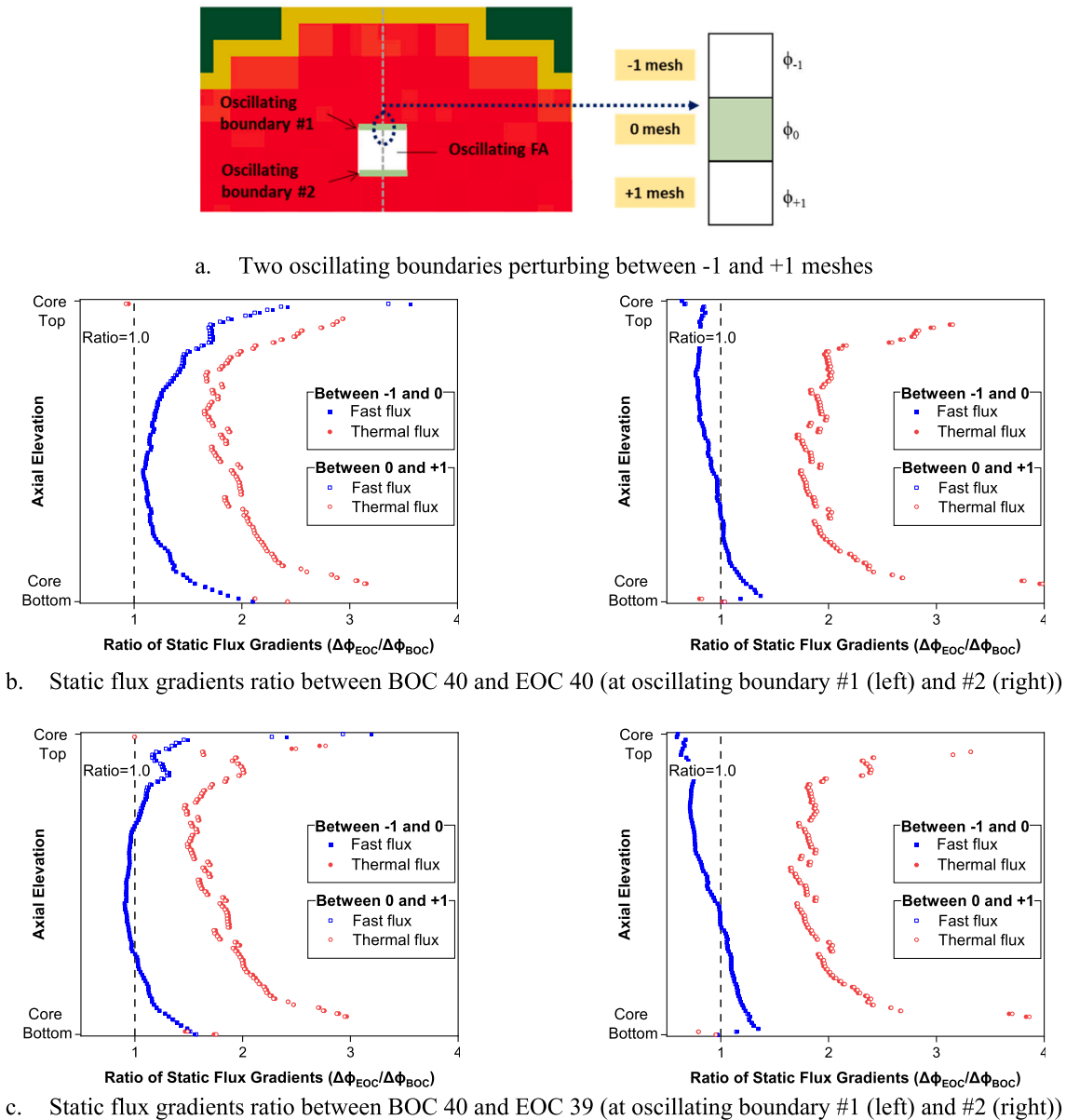a.   Two oscillating boundaries perturbing between -1 and +1 meshes

b.   Static flux gradients ratio between BOC 40 and EOC 40 (at oscillating boundary #1 (left) and #2 (right))

c.   Static flux gradients ratio between BOC 40 and EOC 39 (at oscillating boundary #1 (left) and #2 (right))

Fig. 23. Comparison of ratios of static flux gradients.

is weighted more than at BOC 40 when the assigned location is perturbed, which justifies the increased influence of "location of noise source" on the neutron noise. As will also be explained hereafter, a larger static flux gradient leads to a larger reactivity effect. This itself gives a larger amplitude in the point-kinetic response of the system to the perturbation – see below.

3.4. Importance of sensitivity of phase results

As Fig. 15 and Fig. 20 demonstrate, there is a significant dependence of the phase of the induced neutron noise on both the location of the noise source and the core conditions (cycle and burnup). This is explained by the fact that, in case of a vibrating fuel assembly, the response in neutron noise tends to be out-of-phase between the two regions of the core that originate from the oscillating movement of the fuel assembly. Nevertheless, this out-of-phase behaviour might be masked either partially or totally by the so-called point-kinetic component of the neutron noise, as explained hereafter (Demazière, et al., 2021).

Generally speaking, the induced neutron noise $\delta\phi(\mathbf{r}, t)$ in linear theory can be considered as the sum between a point-kinetic response $\delta P(t)\phi_0(\mathbf{r})$ and the fluctuations of a so-called shape function $\delta\psi(\mathbf{r}, t)$, i.e.

$$\delta\phi(\mathbf{r}, t) = \delta P(t)\phi_0(\mathbf{r}) + \delta\psi(\mathbf{r}, t) \tag{4}$$

In the equation above, $\delta P(t)$ represents the fluctuations of the amplitude factor and $\phi_0(\mathbf{r})$ is the static flux. The amplitude factor and shape functions thus allow retrieving the space- and time-dependent neutron flux as. For this equation, the following normalization condition was used (Bell and Glasstone, 1970):

$$\frac{\partial}{\partial t}\int \phi_0(\mathbf{r})\psi(\mathbf{r}, t)d^3\mathbf{r} = 0 \tag{5}$$

The fluctuations of the amplitude factor are themselves related, in the frequency domain, to the reactivity noise $\delta\rho(\omega)$ via the zero-power reactor transfer function $G_0(\omega)$ as:

$$\delta P(\omega) = G_0(\omega)\delta\rho(\omega) \tag{6}$$

with ω representing the angular frequency. The reactivity noise can

be estimated using first-order perturbation theory as (Bell and Glasstone, 1970):

$$\delta\rho(\omega) = \frac{\int\left[\delta\nu\Sigma_f(\mathbf{r},\omega) - \delta\Sigma_a(\mathbf{r},\omega)\right]\phi_0^2(\mathbf{r})d^3\mathbf{r}}{\int\nu\Sigma_{f,0}(\mathbf{r})\phi_0^2(\mathbf{r})d^3\mathbf{r}} \tag{7}$$

where $\nu\Sigma_{f,0}(\mathrm{r})$ is the static macroscopic fission cross-section multiplied by the average number of neutrons emitted by fission, $\delta\nu\Sigma_f(\mathrm{r},\omega)$ is the corresponding noise and $\delta\Sigma_a(\mathrm{r},\omega)$ is the noise in the macroscopic absorption cross-section. As Eq. (7) demonstrates, asymmetrical perturbations in, e.g., larger flux gradients give a larger reactivity noise, and thus, a larger point-kinetic component of the induced neutron noise – see Eq. (6).

As Eq. (4) shows, the induced neutron noise is made of two terms having fundamentally different spatial dependence:

- The space-dependence of the point-kinetic response is always given by the one of the static flux $\phi_0(\mathrm{r})$ and is thus independent of the applied perturbation. Moreover, one notices that the point-kinetic response has correspondingly the same phase throughout the entire system.
- The space-dependence of the fluctuations of the shape function can be any. In the case of vibrating fuel assemblies, the phase of the shape function between the two out-of-phase parts of the core that arise from the oscillating movement has a discontinuity. Correspondingly, only the fluctuations of the shape functions can carry some space-dependence in the phase.

As demonstrated in (Demazière, et al., 2021), the relative weight of the point-kinetic component in relation to the shape function is responsible for the overall phase response of the induced neutron noise. For an overwhelming point-kinetic component, the phase would be constant throughout the core. Otherwise, the overall phase response will be the result of the competition between the point-kinetic response (having no phase variation) and the shape function (having a phase variation). The differences in relative weights between those two contributions at different core conditions or positions of the vibrating fuel assembly is the main reason why the space-dependence of the overall phase significantly varies accordingly.

In order to study the competing effects between the point-kinetic component of the neutron noise and the shape function component, an additional sensitivity study was carried out. For this purpose, a new loading pattern, based on EOC 39 was created by putting all the fresh assemblies on the outermost ring of the core thus greatly increasing the neutron leakage and the flux gradient in the core (between the inner and the outer part) as shown in Fig. 24.

The thermal neutron noise in the modified core loading is calculated and compared to the original EOC 39 results. The point kinetics and the shape function components of the neutron noise are evaluated for both the original EOC 39 core loading and the maximized neutron leakage one. Regarding the amplitude of the thermal neutron noise, presented in Fig. 25 and Fig. 27, for both core loadings the point kinetics and the shape function components are in opposite directions and compensate each other except near the source of the perturbations. In the original EOC 39 core loading, the phase of the thermal neutron noise (see Fig. 26) varies strongly especially with out-of-phase noise in the northern part of the core. In this case, the phase of the neutron noise is dominated by the shape function component over the point kinetics component, thus confirming the results of (Demazière, et al., 2021). In the modified core loading with increased leakage, the point kinetics component is largely dominating the phase (see Fig. 28), and as expected, no spatial dependency is observed (except, of course, near the source of the perturbations).
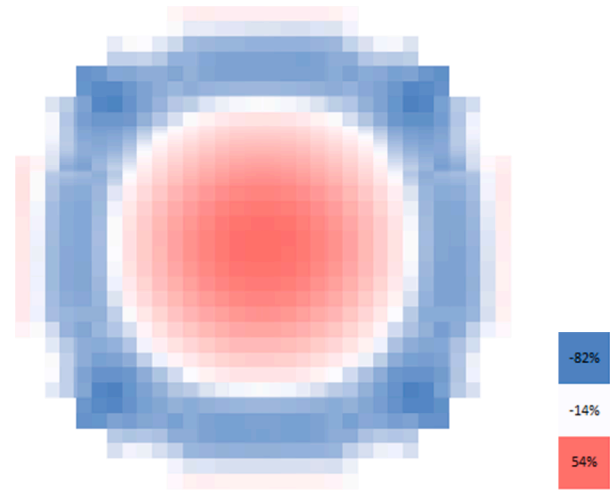

Fig. 24. Relative difference of the thermal flux from the original cycle 39 core loading and the maximized neutron leakage core loading (at the mid-height position of the detector installation).

3.5. Results of the application of the DNN on the sensitivity results (UoL) and the quality detection of source location

We performed the sensitivity analysis of the developed 3D FCNN for perturbations detection and localization. Specifically, we introduced uncertainties on the input parameters, which are used to simulate the noises outputs generated by the vibration of a fuel assembly, based on the CORE SIM + modelling software. The training/validation data sets were not perturbed. Only the testing datasets were perturbed. The detailed parameter uncertainties used for the simulations are summarized in Table 1.

300 trials of simulations under parameters uncertainties were performed for simulating cantilevered fuel assembly vibrations while the recordings by 36 sensors inside the core are obtained. The vibration location on the core cross-section plane is shown in Fig. 29a. The recordings of 36 sensors are used as the input of a trained 3D FCNN (based on a simulated dataset from the Swiss pre-KONVOI reactor without any parameters uncertainties) for classifying/detecting the vibration location.

The ground-truth and the detected vibration locations for one of the simulations used for the sensitivity study by the 3D FCNN on the core cross-section plane with 16-by-16 divisions are shown in Fig. 29b. We can see that the vibration region can be successfully found out by the 3D FCNN network.

Moreover, we performed a more comprehensive evaluation by assessing the vibration classification/localization performance of the proposed 3D FCNN for all 300 simulation scenarios under various simulation input parameters uncertainties, with the results being summarized in Table 4. We can see that the proposed 3D FCNN can achieve both a 100 % classification rate (the vibration type can always be identified) and a 100 % top-3 detection rate (indicating that the top three most likely detected regions cover the ground-truth vibration region). In this Table, top-1 detection means that the actual noise source location was the one which was identified as the most likely and top-2 means that the actual noise source was one of the two most likely detected. Results indicate that the proposed network is robust to the simulation input uncertainties for vibration classification and detection.

4. Conclusion and outlook

The sensitivity of the neutron flux oscillation simulations with CORE SIM+ was analysed for a selected perturbation. Besides variations of the parameters of the neutron noise source and the detectors, uncertainties
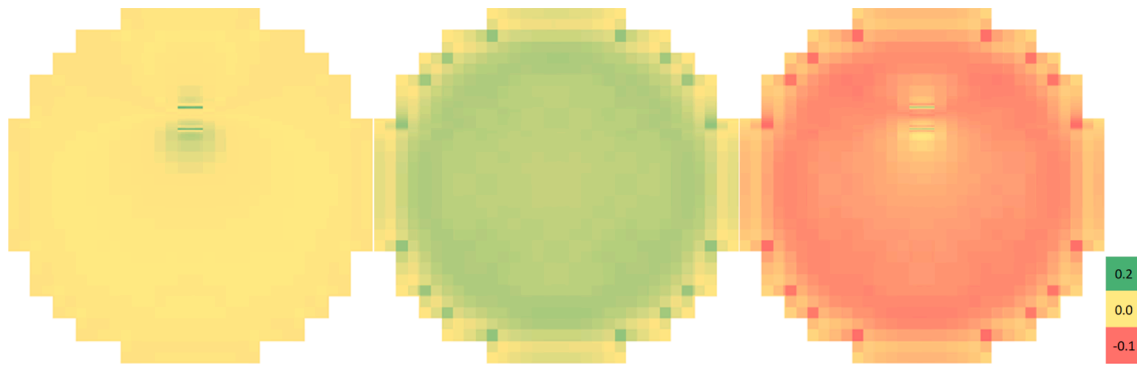
Fig. 25. The amplitude of thermal neutron noise in the original EOC 39 core loading (at the mid-height position of the detector installation) - Left: Total noise, Center: Point kinetics component, Right: Shape function.

Fig. 26. The phase of thermal neutron noise in the original EOC 39 core loading (at the mid-height position of the detector installation) - Left: Total noise, Center: Point kinetics component, Right: Shape function.

Fig. 27. The amplitude of thermal neutron noise in the maximized leakage core loading (at the mid-height position of the detector installation) - Left: Total noise, Center: Point kinetics component, Right: Shape function.
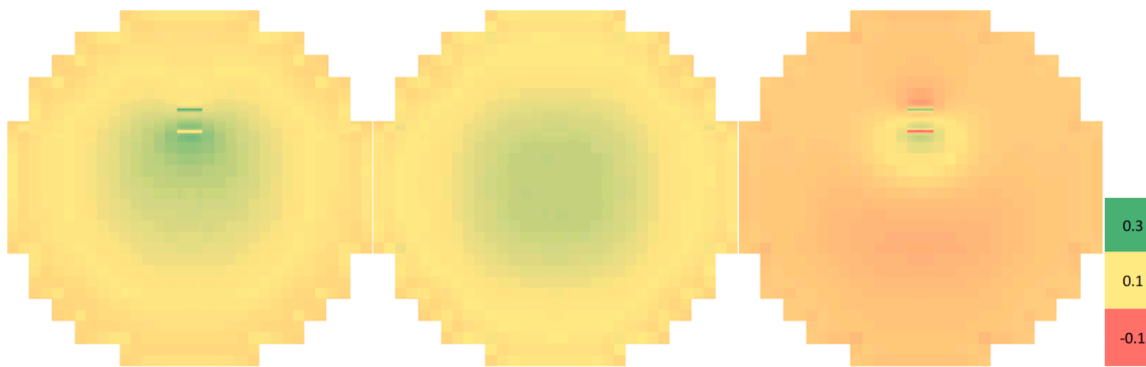
of the neuronic data were derived and used in the sensitivity analysis. The results of these simulations are the location-dependent phase and amplitude of the induced neutron noise. The phase is mostly sensitive to variations of the location of the noise source. For the amplitude, it was found that depending on the core loading and the corresponding static neutron flux field, both the location of the noise source and the amplitude of the fuel vibration can cause comparable quantitative changes. This analysis also reveals that a sufficient deviation from point-kinetics is observed in case of fuel assembly vibrations for large commercial reactors. It was also shown how variations of the core loading pattern can have an impact on this property.

The deviation from point-kinetics is the primary reason why unfolding the noise source from very few detector readings is possible: the spatial signature of the induced neutron noise (amplitude and phase)

is sufficiently different when the noise source position is changed. The dependence on the noise source location can thus be detected by the machine learning architectures. Using the simulation results created by the sensitivity analysis of CORE SIM+ it was found that the 3D-FCNN robustly detects the cause and the location of the perturbation causing the neutron flux oscillations. The variations of the test data via the sensitivity analysis represent uncertainties of the measured data which would be fed into the algorithm when applied to actual plant data. This demonstrates that these uncertainties should have a negligible effect on the detection and localization efficiency of the algorithm.

CRediT authorship contribution statement

J. Herb: Conceptualization, Methodology, Investigation, Writing –

Fig. 28. The phase of thermal neutron noise in the maximized leakage core loading (at the mid-height position of the detector installation) - Left: Total noise, Center: Point kinetics component, Right: Shape function.
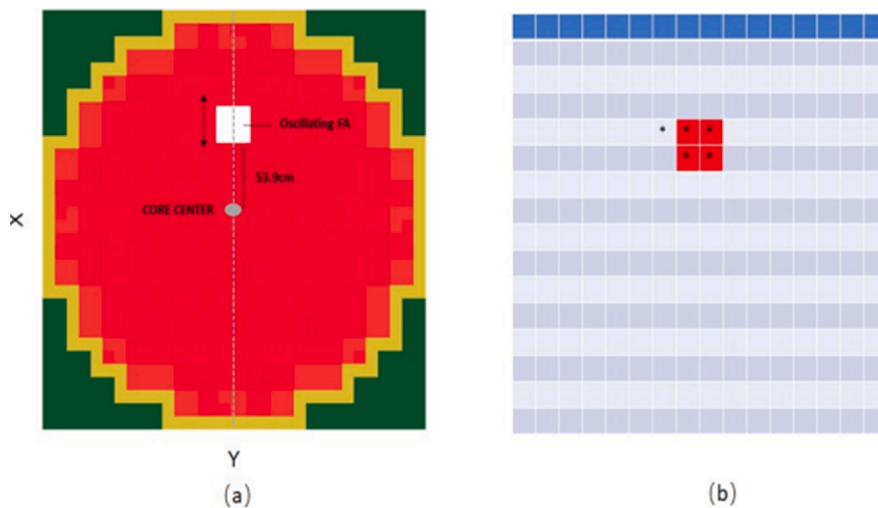

Fig. 29. (a) The vibration location on the cross section plane (b) Ground-truth vibration locations (marked as red) and detected top-5 mostly likely regions (marked as stars) on the cross section plane with 16-by-16 division.

Table 4
3D FCNN results on 300 simulation scenarios under uncertainties.

	Top-1	Top-2	Top-3
Detection rate	42.33 %	96 %	100 %
Classification rate	100 %		

original draft. **Y. Périn:** Conceptualization, Methodology, Formal analysis, Visualization, Writing – original draft. **S. Yum:** Conceptualization, Methodology, Formal analysis, Software, Visualization, Writing – original draft. **A. Mylonakis:** Conceptualization, Methodology, Software, Writing – review & editing. **C. Demazière:** Conceptualization, Methodology, Visualization, Writing – original draft. **P. Vinai:** Conceptualization, Supervision, Methodology, Writing – review & editing. **M. Yu:** Conceptualization, Methodology, Formal analysis, Visualization, Writing – original draft. **J. Wingate:** Conceptualization, Methodology, Formal analysis, Writing – review & editing. **M. Hursin:** Conceptualization, Supervision, Methodology, Writing – review & editing.

Declaration of Competing Interest

The authors declare that they have no known competing financial interests or personal relationships that could have appeared to influence the work reported in this paper.

Data availability

The authors do not have permission to share data.

References

Anon., n.d. *SPSS Tutorials: Pearson Correlation.* [Online] Available at: https://libguides.library.kent.edu/SPSS.

Bell, G., Glasstone, S., 1970. Nuclear Reactor Theory. Van Nostrand Reinhold Company, New York, USA.

Bläsius, C., Herb, J., Sievers, J., Knospe, A., Viebach, M., Lange, C., 2022. Mechanical model for the motion of RPV internals affecting neutron flux noise. Annals of Nuclear Energy 176, 109243.

Bluman, A.G., 2009. Elementary Statistics: A Brief Version, 7 ed. McGraw-Hill, New York.

Caliva, F., De Ribeiro, F. S., Mylonakis, A., Demazière, C., Vinai, P., Leontidis, G., Kollias, S., 2018. A deep learning approach to anomaly detection in nuclear reactors. 2018 International Joint Conference on Neural Networks (IJCNN).

Conover, W.J., 1980. Practical Nonparametric Statistics, 3rd ed. John Wiley & Sons, New York.

Demazière, C. & Dokhane, A., 2019. *Description of scenarios for the simulated data,* s.l.: CORTEX Technical Report D3.1.

Demazière, C., Mylonakis, A., Vinai, P., Durrant, A., De Sousa Ribeiro, F.., Wingate, J., Leontidis, G., Kollias, S., 2020. Neutron Noise-based Anomaly Classification and

Localization using Machine Learning. International Conference on Physics of Reactors (PHYSOR) 2020.

Demazière, C., Rouchon, A., Zoia, A., 2021. Understanding the neutron noise induced by fuel assembly vibrations in linear theory. Virtual Meeting, Proceedings of the International Conference on Mathematics and Computational Methods Applied to Nuclear Science and Engineering (M&C2021).

Durrant, A., Leontidis, G., Kollias, S., 2019. 3D convolutional and recurrent neural networks for reactor perturbation unfolding and anomaly detection. EPJ Nucl. Sci. Technol. 5, 20.

Gösgen, 2018. *Gösgen Contribution to D 4.2,* s.l.: CORTEX Internal Technical Report.

Kajuri, S., 2018. *Application of Hypothesis Testing and Spearman's rank correlation coefficient to demystify Suicides worldwide.* [Online] Available at: https://towardsdatascience.com/application-of-hypothesis-testing-and-spearmans-rank-correlation-coefficient-to-demystify-b3a554730c91.

Kaul, P., De Martini, D., Gadd, M. & Newman, P., 2020. *RSS-Net: Weakly-Supervised Multi-Class Semantic Segmentation with FMCW Radar,* s.l.: arXiv preprint arXiv:2004.03451.

Kernkraftwerk Gösgen-Däniken AG (KKG), 2016. *Technical Brochure 'Technology and Operation.* [Online] Available at: https://www.kkg.ch/upload/cms/user/KKG_TB_englisch_2016.pdf [Accessed 20 February 2022].

Mylonakis, A., Vinai, P., Demazière, C., 2021. CORE SIM+: A flexible diffusion-based solver for neutron noise simulations. Ann. Nucl. Energy 155, 108149.

Ramsey, P.H., 1989. Critical values for spearman's rank order correlation. J. Educ. Stat. 14 (3), 245–253.

Rearden, B.T., Jessee, M.A., 2016. SCALE Code System, ORNL/TM-2005/39, Version 6.2.1. Oak Ridge National Laboratory, Oak Ridge, TN, USA.

Sarrazin, F., Pianosi, F., Wagener, T., 2016. Global sensitivity analysis of environmental models: convergence and validation. Environ. Model. Softw. 79, 135–152.

Wang, B., et al., 2019. Deeply supervised 3D fully convolutional networks with group dilated convolution for automatic MRI prostate segmentation. Med. Phys. 46, 1707–1718.

Yum, S., et al., 2022. Uncertainty analyses of neutron noise simulations in a zero-power reactor. Ann. Nucl. Energy 174, 109157.

Yum, S. & Perin, Y., 2021. *Result of the sensitivity analyses,* s.l.: CORTEX Technical Report D4.5.